Double Cation Substitution of CZTSSe Constituents to Reduce Detrimental Defects Clusters and Improve Device Performance

Jeffrey Chin

A thesis

submitted in partial fulfillment of the

requirements for the degree of

Master of Science

University of Washington

2020

Committee:

Hugh Hillhouse

Qiuming Yu

Program Authorized to Offer Degree:

Chemical Engineering

University of Washington

Abstract

Double Cation Substitution of CZTSSe Constituents to Reduce Detrimental Defects Clusters and Improve Device Performance

Jeffrey Chin

Chair of the Supervisory Committee:
Hugh Hillhouse
Department of Chemical Engineering

Solution processed thin-film photovoltaic (PV) technology is poised to be the future of manufacturing standard for commercially available solar energy modules due to the substantially low estimated capital expenditure (CAPEX) required. Over the decades, the concept of high efficiency CZTSSe has enticed researchers but always eluded their grasps. This report explores improving the device performance metrics of CZTSSe with the goal of improving the PCE in hopes that it become industrially disruptive to the currently adopted technologies. The approach taken in this research was to conduct double cation alloying with elements shown in literature to have beneficial impacts for CZTSSe device performance with the hypothesis that the combination would be complementary. First, we investigated the combination of small stoichiometric substitutions of Cu with Ag and Zn with Mn so that the resulting stoichiometry would resemble $(Ag_x,Cu_{1-x})_2(Mn_yZn_{1-y})Sn(S,Se)_4$. Second we investigated the double cation substitution of Cu with Ag and Sn with Ge so that the already proven effects of Ge incorporation could be correlated with the effects of Ag. Collectively, the work included in

this report demonstrates considerable progress exploring uncharted avenues toward increasing the performance of CZTSSe. By attempting a new approach to understanding optoelectronic performance and reliability in CZTSSe the goal of high efficiency CZTSSe may soon be attainable.

1. Introduction

Solution processed thin-film photovoltaic (PV) technology is poised to be the future of manufacturing standard for commercially available solar energy modules. The estimates of the difference in capital expenditures (CAPEX) for the production from current technologies, such as c-Si, transitioning to similarly efficient (PCE) solution processed thin-film modules there is an estimated cost savings of over an order of magnitude when normalized with power output per duration [1]. But the continuing issues with solution processed PV technology are that are half as efficient as industry based modules or that the chemical constituents are very toxic to the populous and environment. Other disadvantages for leading solution processed methods include factors of the low availability of the required elements and also the stability of the film in ambient conditions make those respective candidates unlikely industry replacements.

$Cu_2ZnSn(S,Se)_4$ (CZTS) solar cells are advantageous compared to the aforementioned solution processed thin-films field sticking points, but lack a high PCE to disrupt the natural order of the PV module production world. Chalcogenide solar cells are modeled from earth abundant and naturally occurring kesterite geological minerals composed of low hazard and earth abundant copper, zinc, tin, sulfide, and selenide materials as a P-type absorber layer. The stoichiometry Cu_2ZnSnS_4, which has been the starting point for multiple avenues of kesterite research for over two decades has a bandgap of ~1.51eV. In the research field, the acronym CZTS ambiguously refers to the chalcogenide elements as “S”, but more specifically depending on the fabrication could be elementally sulfide Cu_2ZnSnS_4, selenide $Cu_2ZnSnSe_4$ (Eg=~0.94eV), or sulfo-selenides $Cu_2ZnSn(S_x,Se_{1-x})_4$. The sulfo-selenide stoichiometry has been studied in depth and by varying the ratio of S/(S+Se) the Eg can be effectively “tuned” to different values between the value of sulfide and selenide. The best devices in the CZTS field have been rich in selenium and a ratio of 5-10% sulfur to the total chalogens. The highest CZTS PCE independently measured was fabricated by an IBM research effort and achieved 12.6% efficiency, at an Eg of 1.13 eV [2].

The Shockley-Queisser (SQ) detailed balance theoretical limit delineates the maximum possible efficiency at a certain Eg for a single p-n junction behaving as an ideal diode under illumination of the Air Mass (AM) 1.5 solar spectrum [3]. At Eg=1.13eV, the Shockley-Queisser theoretical limit is approximately 33.5%, meaning that the record CZTS device has only attained 38% of potential maximum efficiency. Evaluating the record CZTS metrics of open circuit-voltage (V_{OC}), short-circuit current (J_{SC}), and fill factor (FF) are normalized by the respective Eg SQ theoretical V_{OC}, J_{SC} (V_{OC}^{SQ}, and J_{SC}^{SQ}), and FF. Upon comparison of these metrics it becomes very apparent (especially juxtaposed to other technologies) that the CZTS deficient PCE is primarily a function of V_{OC} (V_{OC}/V_{OC}^{SQ}=58%). V_{OC}/V_{OC}^{SQ} serves as an important metric to normalize the experimentally observed Voc's with materials of varying bandgaps to evaluate potential performance. As Eg increases the Voc^{SQ} increases linearly but at a lesser slope; Voc^{SQ} at 300K can be extracted by the linear model in equation 1. Equation 2 is commonly referred to as the "Voc deficit" and represents the differential in the Eg and Voc that is due to the "untapped" potential at a given Eg. It is important for the Voc deficit to be minimized in CZTS materials, but Voc/Voc^{SQ} is a more useful metric when engineering materials of different Eg values.

$$V_{OC}^{SQ} = 0.932 \times \frac{Eg}{q} - 0.167 \tag{1}$$

$$V_{OC}^{deficit} = \frac{Eg}{q} - V_{OC} \tag{2}$$

Many articles will report higher CZTS Voc values compared to that of the record device (513 mV), but their material is at a much larger Eg and therefore when normalized with the Voc^{SQ} will fall short and as expected the device will not have a record efficiency either.

Researchers have hypothesized many different theories on the root cause or causes of the low V_{OC}, including Sn induced deep defect clusters, Cu_{Zn} / Zn_{Cu} site disorder, and band-tailing to name the most prevalent, but few have shown progress to improve the V_{OC} deficiency [4]. The physical and chemical processes which lead to high V_{OC}, high PCE solution-processed

CZTS devices are still being discovered, the research presented in this report explore the combination of lessons learned from the CZTS research community.

The Periodic table group representation of CZTS is I_2-II-IV-VI_4 and there have been a multitude of research efforts to substitute elements into the structure and study the effects. One very informative research efforts that illustrate that the low V_{OC} is a solvable challenge employed a gradient of germanium alloying into the CZTS group IV metals the V_{OC} will increase to 580 meV which is the highest published value for CZTS and improves the V_{OC}/V_{OC}^{SQ} = 63% compared to the 58% attained by the current champion device, however only achieved 11.0% efficiency. It is hypothesized that since Ge^{4+} has an approximate ionic radii of 53 pm and Sn^{4+} has an approximate ionic radii of 69 pm that with small replacements with Ge (20-40% Ge/(Ge+Sn)) that Sn-related defects such as Zn_{Sn} and Cu_{Sn} should be suppressed [5]. Silver alloying has also shown promise as an alloying candidate and by small incorporations of Ag (10-30% Ag/(Cu+Ag)) devices can be usually achieve over 10% efficiency. Cu^{+} has an approximate ionic radii of 74 pm and Ag^{+} has a larger approximate ionic radii of 115 pm and the impact has been shown to be that Cu_{Zn} defects are reduced and experimentally a reduction of band-tailing has been observed [6]. Ag alloying has not shown significant improvements in Voc, but rather PCE and suggests that Ag incorporation is favorable for the interface with CdS buffer layer. The replacement of Cu by Ag and Sn by Ge has been proposed in this work to avoid Cu_{Zn} antisite defects formed due to the random distribution of Cu and Zn in CZTSSe films, Sn-related deep defects harmful to Voc, and reduce band-tailing.

In addition to investigating the combination of using Ag and Ge as a double cation substitution strategy. Our research group proposed the additional investigation into the combination of Ag and Mn double cation substitution. Mn as an alloying adduct into CZTS has been in effort to reduce Zn related point defects and alloying experiments have also shown to promote grain growth and enhance grain boundaries in CZTS [7]. Zn^{2+} has an approximate ionic radii of 74 pm and Mn^{2+} has an approximate ionic radii of 83 pm so the replacement effect is hoped to be that similar to Cu with Ag. This double cation substitution was investigated as an alloying gradient with the expectation not that the Voc would increase but that the PCE on already proven AgCZTS compositions would increase. The replacement of Cu by Ag and Mn by Zn has been proposed in this work to avoid Cu_{Zn} anti-site defects formed due to the random distribution of Cu and Zn in CZTSSe films.

If shown positive improvements with he absorbed layer engineering with Ag + Ge cation substitution and Ag + Mn cation substitutions it is plausible that the direction for a design of experiments that could fabricate a champion CZTS device that results from a triple Ag + Mn + Ge cation substitution. To maintain the focal point of this research is to engineer the absorber layer with two independent double cation substitution studies the subsequent layers in the device fabrication (CdS, i-ZnO and ITO) need to be engineered to be reproducible for consistency between fabrication batches. We have chosen methods that allow the fabrication results to mimic IBM's record device reported band alignment. It is important to note that by incorporating the cations of Ag, Mn, and Ge have been shown to increase the Eg of CZTS [8]. Since partial double cation substitutions do not appear in CZTS literature the task becomes more challenging because at the CZTS/CdS interface deviation from the optimal conduction band-offset could lead to interfacial recombination. This device defect would detract from analysis of the quasi-fermi level splitting in the absorber layer. Therefore, quantities engineered in the alloying effort are approximated (without doing DFT calculations) so that the resulting absorber layer has a material property of Eg= ~1.13 eV.

Having explained the potential of the double cation substitutions and the physical and chemical understanding it could unlock, the true unspoken goal of this research lingers that we wish to dethrone the long-standing hydrazine-based solution processed CZTS PCE. If this work is able to contribute to that goal it increases the likeliness and practicality of industrial adoption solution processed thin-film CZTS.

2. Experimental Setup and Methods

The procedures and characterization methods described below were chosen specifically based on desire to optimize the absorber layer. It is important to note that the steps 2.1 through 2.5 represent a cheap solution based methodology whereas step 2.6 required expensive tool use time to complete the device fabrication. The cost trade off in this particular study is that it would allow concentration on the substituted stoichiometry of the CZTS absorber layer by keeping the subsequent layers of i-ZnO, ITO, and metal contacts with little variance from device to device.

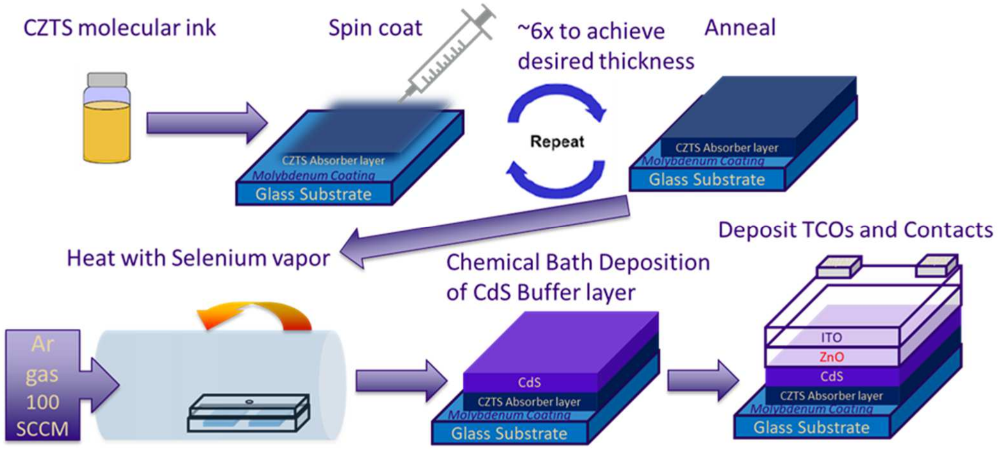

Figure 2-1. Solution processed thin films methodology schematic summarizing subsections 2.1 through

2.1 Precursor CZTS Molecular Ink Synthesis.

Target co-alloying ratios of Ag and Ge were estimated by extrapolating trends from single alloying Ag and Ge research to achieve a predicted bandgap close to that of 1.13 eV of CZTS/CdS apparent optimal conduction band-offset. Precursor solutions of CZTS with respective targeted alloying ratios as described by were synthesized by the combination of N,N Dimethylforminide as solvent; 0.5 M lithium chloride was added as a dopant [9]; and the addition of calculated solids thiourea (TU), copper(II) acetate, zinc chloride, tin(II) chloride, and silver chloride (as applicable), and liquid germanium (IV) chloride. All metal salts used are anhydrous and ≥99.999% trace metals basis. Synthesis is conducted in a contained N_2 rich (O_2 levels maintained below 25 ppm) glovebox environment and the precursor adducts are allowed to dissolve into solution at room temperature under constant stirring. The adducts were calculated to target ratios of periodic group and elemental ratios and accounts for observed elemental losses from subsequent thermal treatments to maintain targeted I_2-II-IV-VI_4 stoichiometry [10]. In addition to the alloying ratios we used Collord, et. al's article to calculate CZTS metal group ratios to be added: TU/Total metals=400%, I/Total metals=43%, II/Total metals=29.2%, IV/Total metals=27.8%, I/(II+IV)=75%, and II/IV=105% [10]. These ratios prevent the formation of low band gap ternary phases (for example Cu_2SnS_3) which are favored in Cu-rich compositions and are potential causes for Voc deficit of devices prepared under such conditions [4]. Because of that, these ratios are found to be the optimum for highest efficient CZTSSe devices [1,5–7]

2.2 Precursor Film Deposition via Spin Coating.

The chalcogenide molercular ink films were deposited onto Mo-coated soda lime glass (MSLG) substrates 2.5 x 2.5 cm. Previously, substrates were cleaned by sequentially washing in, deionized water, acetone, and 2-propanol, under sonication, and dried with N_2. The precursor solutions were filtered using a 1.0 μm PTFE syringe filter and spin-cast onto MSLG substrate at 2000 rpm for 60 s.

2.3 Absorber Layer Static Annealing.

From the spin coating instrument the freshly coated substrates were onto a hot-plate preheated to an annealing temperature of 300°C and allowed to statically anneal for 90s. The substrate is allowed to cool via ambient thermal convection and then steps 2.2 and 2.3 are iteratively repeated to increase the precursor film thickness. Profillometry was used on cooled reference precursor films to confirm accumulated thickness. The procedure was repeated 6 times to obtain a film thickness equal to ~1200 nm.

2.4 Selenization of CZTS Precursor Film.

Introduction of selenium vapor to the precursor films removes impurities (primarily carbon based) and replaces sulfur with selenium in the crystalline structure of the CZTS. Selenization is conducted in a glass tube furnace in argon rich environment. The precursor substrates are held in the tube furnace inside a specialty graphite box loaded with elemental selenium pellets (~5mm), which once heat is applied will quickly vaporize creating a selenium rich environment inside of the box. The tube containing the graphite box is maintained with an Ar rich flow of 100 cm^3 min^{-1} throughout the reaction. The tube furnace is set point is 500°C and the selenization is allowed to progress for 20 minutes before aborting the heating program and allowing the system to cool to ambient temperature.

2.5 Chemical Bath Deposition of Cadmium Sulfate (CdS) Buffer Layer.

A buffer layer of CdS is deposited onto the selenized absorber to protect the absorber layer. A Chemical bath of 183 ml of deionized H_2O, 25 ml of 0.015 M $CdSO_4$ solution, 12.5 of 1.5M thiourea solution, and 31.25 ml of NH_4OH are combined in a jacketed beaker that is pre-heated to 65°C and the mixture is continuously stirred on a stir-plate. Using a substrate holder the selenized substrates are submerged into the chemical bath for 10 min. The thickness of the CdS deposition is ~40 nm [11].

2.6 Device Fabrication via Transparent Conducting Oxide Layers Sputtering and Evaporating

Device fabrication steps including sputtering and evaporating are conducted at the Washington Nanofabrication Facility for reliability of reproducible results from this fabrication step. Intrinsic n-type zinc oxide (ZnO) layer of 70 nm is sputtered followed by sputtering a 300 nm layer of (ITO). Subsequent high vacuum e-beam evaporation depositions of 70 nm nickel and 2 um aluminum metal contacts are conducted using shadow masks that produces an array of 35 devices per each substrate. A ~110 nm thick MgF layer can also be deposited in the evaporator at this time as an anti-reflective coating to improve device quantum yield and current density. Final device preparation includes manually scribing lines delineated by the shadow mask to isolate each of the 35 devices (~0.105-0.115 cm^3 active area) using a razor and then soldering indium is around the perimeter of the substrate as the electrode to the Mo back-contact.

2.7 Device Characterization and Analysis

(SEM) micrographs were collected with an FEI Sirion XL30 microscope using a 5 kV accelerating voltage. Energy-dispersive X- ray spectroscopy (EDX) data were collected with an Oxford EDX detector using an accelerating voltage of 20 kV. SEM allows us to image morphological features as small as 10 nm in ultra-high resolution to qualitatively describe the bulk regions surface grain size and density. In conjunction with the SEM we then use an EDX detector to verify the stoichiometric metal ratios to determine elemental losses due to annealing or selenization. SEM and EDX can also be taken of a cut cross-section of a sample to visualize the presence and composition of fine-grain layers.

Photoluminescence (PL) measurements were conducted using a LabRam HR800 Raman instrument equipped with a 785nm IR laser, 10x optical objective lens, and InGaAs liquid N_2 cooled detector. Absolute Intensity PL (AIPL) spectral analysis can be performed by collecting a calibration curve from a known emission source, such as a NREL certified black-body IR source at a certain temperature, to create a spectral flux correction factor that removes artifacts from the PL data caused by filters and varying efficiency regions of the detector. AIPL measurements of samples allows us to reliably predict the performance of a device by calculating the Eg and quasi-fermi level splitting (QFLS) which represents a maximum attainable Voc for the material. The QFLS can be simply corrected to a one sun excitation which is indicative of the V_{OC} of completed device and further we can compare substrates of different calculated bandgaps by normalizing to V_{OC}/V_{OC}^{SQ} (Chi [%]).

Glow discharge optical emission spectroscopy (GDOES) was conducted using a Horiba GD-Profiler 2. GDOES gives rapid depth-resolved elemental analysis with down to 5 nm resolution. The instrument uses an Ar plasma to sputter a 4 mm diameter crater into the sample, and uses atomic emission spectroscopy to identify the material being sputtered away. GDOES allows us to quantify the carbon content remaining in the absorber layer post selenization by sputtering Ar plasma through the sample and by calibrating the spectral data we can define the elemental profiles as a function of depth.

X-ray diffraction (XRD) was performed on the films with a Bruker D8 Discover. The source was a Cu Kα X-ray with an incident wavelength of 1.54059 Å and montel collimating optics to remove Kβ. A round collimator of diameter 0.5 mm was used. The detector was a 2D Pilatus 100k detector with radius 15.4 cm and an opening of 2.6°. XRD is an effective tool to quickly determine the presence of multiple phases in the absorber layer as result from the fabrication process. XRD information can also be refined and using the peak information one can determine lattice constants using Bragg's law.

Current−voltage (JV) measurements were performed in ambient conditions using a Keithley 2400 source- measure unit. JV measurements used a Newport AAA Oriel Sol3A solar simulator emitting 1000 W/m^2 at standard conditions (25 °C and AM1.5G), calibrated with a Newport Si reference cell. Completed devices are tested under a solar simulator by conducting a sweep by applying a forward bias voltage and measuring the current while under 1 sun excitation which produces a current-voltage characteristic (JV) curve that is analyzed using the Lambert W-function to extract device performance. Devices of special interest can be measured using the external quantum efficiency setup to reveal the percentage of electron hole pairs are collected as a function of photon wavelength. EQE measurements are calibrated with certified Si and Ge photodiodes.

UV-Vis spectral measurements were collected with a Perkin Elmber Lambda 1050 spectrometer equipped with a Peltier-cooled InGaAs detector for IR, PbS detector for the NIR, and a tungsten-halogen lamp as an emission source. To utilize this apparatus the films were also deposited on soda lime glass (SLG) substrates using the same method as described above in sections 2.1-2.4. The transmitance of the films were acquired between 500-1800 nm using a UV-Vis-NIR spectrophotometer and integrating sphere unit.

3. Results and Discussion

3.1 Elemental analysis of Ag, Mn, and Ge –substituted CZTSSe films

All the films were prepared under Cu-poor, I/(II+IV) = 0.75, and Zn-rich conditions, II/IV = 1.05. These ratios prevent the formation of low band gap ternary phases (for example Cu2SnS3) which are favored in Cu-rich compositions and are potential causes for Voc deficit of devices prepared under such conditions [12]. Because of that, these ratios are found to be the optimum for highest efficient CZTSSe devices [2, 5, 13,14]. The elemental analysis shows that the Cu-poor condition is maintained throughout all compositions with I/(II+IV) approximately 0.75. Although II/VI elemental ratio varied between 1.06 and 1.19, all the sample are also Zn-rich. The CZTS transformation to CZTSSe by selenization is confirmed by the S/(S+Se) ratios. The chalcogenide composition for the Ag and Mn CZTSSe films are 5-10% sulfide and respectively 90-95% selenide. Table 1 below lists the results obtained from SEM/EDX measurements.

The elemental analyses also confirm the incorporation of the Ag, Ge and Mn into the CZTSSe films. The atomic ratio of the extrinsic elements are represented by the Ag/(Cu+Ag),

Table 1. *Semi-quantitative elemental analysis of the Ag, Ge, and Mn-alloyed CZTSSe calculated by energy dispersive x-ray spectroscopy .*

	Nominal Composition		**Semi-quantitative elemental analysis by EDX**				
Sample	**Ag/ (Ag+Cu)**	**Mn/ (Mn+Zn)**	**Ag/ (Ag+Cu)**	**Mn/(Mn+Zn)**	**II/IV**	**I/(II+IV)**	**S/ (S+Se)**
CZTSSe	**0**	**0**	0	0	1.12 ± 0.03	0.77 ± 0.01	0.060 ± 0.004
i	**0.15**	**0**	0.170 ± 0.004	0	1.06 ± 0.04	0.76 ± 0.03	0.055 ± 0.001
ii	**0.15**	**0.08**	0.170 ± 0.002	0.090 ± 0.002	1.08 ± 0.02	0.77 ± 0.01	0.050 ± 0.003
iii	**0.15**	**0.15**	0.170 ± 0.003	0.180 ± 0.005	1.17 ± 0.02	0.76 ± 0.01	0.089± 0.009
iv	**0.15**	**0.22**	0.15 ± 0.01	0.220 ± 0.005	1.19 ± 0.02	0.77 ± 0.01	0.092 ± 0.002
v	**0**	**0.15**	0	0.18 ± 0.06	1.08 ± 0.02	0.75 ± 0.02	0.106 ± 0.009
vi *	**0.08**	**0.15**					
vii	**0.22**	**0.15**	0.210 ± 0.002	0.120 ± 0.006	1.09 ± 0.01	0.74 0.01	0.054± 0.007

Sample	**Ag/ (Ag+Cu)**	**Ge/ (Ge+Sn)**	**Ag/ (Ag+Cu)**	**Ge/(Ge+Sn)**	**II/IV**	**I/(II+IV)**	**S/ (S+Se)**
CZTSSe	**0**	**0**	0	0	1.12 ± 0.03	0.77 ± 0.01	0.060 ± 0.004
i	**0.15**	**0**	0.170 ± 0.004	0	1.06 ± 0.04	0.76 ± 0.03	0.06 ± 0.01
viii	**0**	**0.3**	0	0.303 ± 0.005	1.04 ± 0.01	0.77 ± 0.02	0.09 ± 0.01
ix	**0.1**	**0.3**	0.110 ± 0.002	0.310 ± 0.004	1.05 ± 0.02	0.75 ± 0.02	0.09 ± 0.01
x	**0.2**	**0.35**	0.227 ± 0.007	0.32 ± 0.01	1.02 ± 0.02	0.73 ± 0.01	0.094 ± 0.002
xi	**0.3**	**0.2**	0.31 ± 0.01	0.24 ± 0.01	1.13 ± 0.02	0.82 ± 0.01	0.09 ± 0.02

*Composition confirmation contained errors so values are not reported for this section

Ge/(Ge+Sn), and Mn/(Mn+Cu). The values presented by the films post selenization are close to the ratio values targeted according to the calculated precursors to prepare the molecular inks, which means that no significant amounts of Ag, Ge, nor Mn are lost during annealing and selenization steps. The SEM/EDX data also serves to validate the fabrication methodology to produce homogenous films. Phase purity is verified by XRD measurements.

3.2 Double Cation Substitution Bandgap Tuning

To evaluate the impact of double cation substitution on the optical properties of the absorber layer selenized films on SLG were measured using the UV-Vis to acquire transmittance data which could be then analyzed to determine absorption coefficients for each composition. Tauc plots, Figure 3-1, were then made from that data to extract Eg from the bulk of the material. Another method used to determine Eg can be preformed from EQE measurements. This is particularly useful measurement because it more accurately illustrates the optical properties unique to the ~0.1 cm^2 area of the device that has been isolated from the bulk of the substrate by manual scribing.

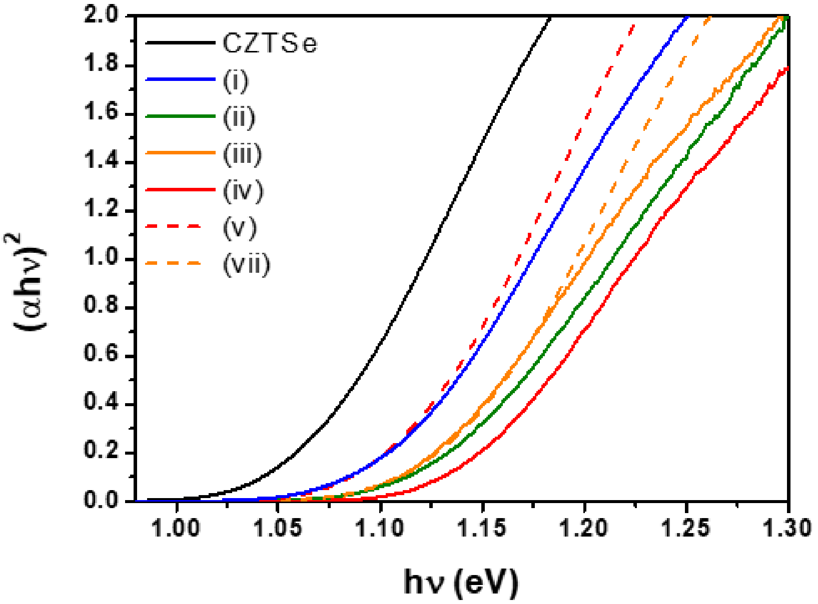

Figure 3-1. *Tauc plot for CZTSe, $(Ag_x,Cu_{1-x})_2(Mn_{0.15},Zn_{0.85})Sn(S,Se)_4$ and $(Ag_{0.15},Cu_{0.85})_2(Mn_z,Zn_{1-z})Sn(S,Se)_4$ films produced from UV-Vis transmittance measurements with duplicate films prepared on SLG.*

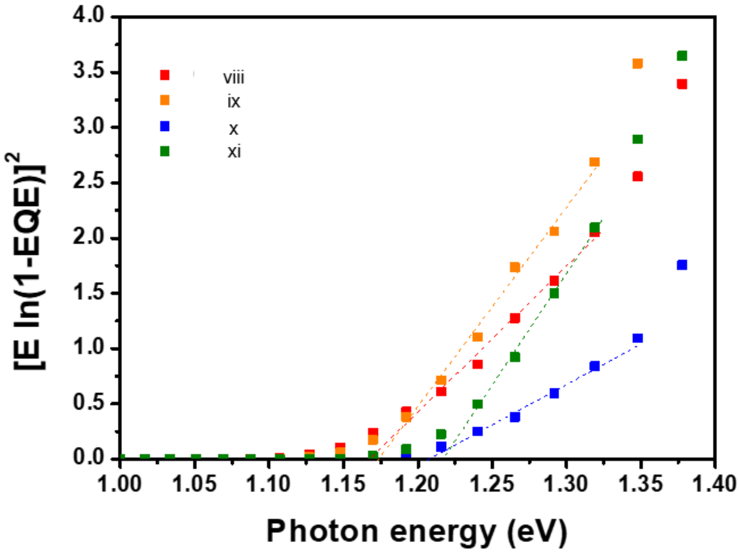

Figure 3-2. *Low energy tail extraction of Eg from EQE data for $Cu_2Zn(Ge_{0.3}Sn_{0.7})(S,Se)_4$ (in red), $(Ag_{0.1},Cu_{0.9})_2Zn(Ge_{0.3}Sn_{0.7})(S,Se)_4$ (in orange), $(Ag_{0.2},Cu_{0.8})_2Zn(Ge_{0.35}Sn_{0.65})(S,Se)_4$ (in blue) and $(Ag_{0.3},Cu_{0.7})_2Zn(Ge_{0.2}Sn_{0.8})(S,Se)_4$ (in green). Measurements plotted taken from highest PCE device per composition.*

Table 2. Eg extracted from various methods (Photoluminescence, UV-Vis, and EQE)

Sample	Ag/(Ag+Cu)	Mn/(Mn+Zn)	PL	UV-VIS	EQE	Voc^{SQ} (V)
CZTSSe	**0**	**0**	0.98	1.05		0.812
i	**0.15**	**0**	1.12	1.10		0.858
ii	**0.15**	**0.08**	1.11	1.11		0.868
iii	**0.15**	**0.15**	1.12	1.12		0.877

iv	**0.15**	**0.22**	1.13	1.14		0.895
v	**0**	**0.15**	1.12	1.09		0.849
vi	**0.08**	**0.15**		1.09		0.849
vii	**0.22**	**0.15**	1.17	1.12		0.877
Sample	**Ag/(Ag+Cu)**	**Ge/(Ge+Sn)**	**PL**	**UV-VIS**	**EQE**	**Voc^{SQ} (V)**
CZTSSe	**0**	**0**	0.98	1.05		0.812
i	**0.15**	**0**	1.12	1.10		0.858
viii	**0**	**0.3**	1.10		1.13	0.886
ix	**0.1**	**0.3**	1.11		1.16	0.914
x	**0.2**	**0.35**	1.17		1.19	0.942
xi	**0.3**	**0.2**	1.17		1.21	0.961

Collectively the analyzed Eg’s from each method agree with each other with deviation no greater than ±50 meV which is approximately the value of 2kT. 50meV is a small difference in energy levels but since the percentage of cation alloying is small and two dimmentional accepting one method over another could have a substantial impact for double substitution performance trend analysis. To maintain consistency the to evaluate VocSQ at a given temperature, Eg’s extracted from UV-Vis, as shown in Figure 4, were used for the Ag and Mn alloyed samples. For the Ag and Ge alloyed samples, since EQE measurements, as shown in Figure 5, were taken of the best preforming devices, Eg’s extracted from EQE were used to increase the accuracy in reporting Voc/VocSQ. PL measurements of Eg are reported but not used because of issues with the calibration of the instrument therefore making the values unreliable. Another disadvantageous aspect of PL measurements to characterize the material data is that the laser spot (approximately $8x10^{-7}$ cm^2) is much smaller than the active area of fabricated device (approximately $1x10^{-1}$ cm^2). Any compositional heterogeneity across the bulk region will result in varying values. Since UV-Vis and EQE are both meaesurments of bulk regions they better representation of the material properties when correlating with device performace.

The band gap energy (as shown in Table 2) of the CZTSSe films also increase with Ag and Mn alloying. The Mn and Ag substitution resulted in an increase of 40 meV to 88 meV in the band gap in comparison to the pure-CZTSSe (1.050 eV). The Eg value for

$(Ag_{0.15},Cu_{0.85})_2ZnSn(S,Se)_4$ (1.103 eV) is lower than the one for $Cu_2(Mn_{0.15},Zn_{0.85})Sn(S,Se)_4$ (1.091 eV), which means Ag has a large effect on Eg increase than Mn. This agrees to our hypothesis generated from literature studies of single cation and considering the ionic radii differential of Ag to Cu is much larger than that of Mn to Zn.

The band gap energy (as shown in Table 2) of the CZTSSe films also increase with Ag and Ge alloying. The increase in energy level is also likely dominated by Ag alloying for the reasons stated above but since the compositions were not linear additions of alloying as with the experimental design of Ag + Mn alloying it is difficult to conclusively determine from this data. For future work it is important to note that the higher double cation substitutions of Ag + Ge resulted in Eg's higher than the target for the device conduction band offset. If more work were to be conducted in this double alloying parameter space in the future, I would recommend limiting Ag content in the range of 5-20% Ag/(Ag+Cu) and Ge content in the range of 25-35% Ge/(Ge+Sn).

3.3 Solar cell performance under 1 Sun illumination

Current-voltage (JV) sweeps were measured under forward bias, room temperature, and 1 Sun (AM1.5G) conditions. The collected curves were then analyzed using the Lambert W-function to extract the photovoltaic performance for each composition fabricated. Table 3, below, summarizes the photovoltaic metrics observed. To evaluate if the increased Voc is associated to the suppression of the relative defects, the ratio Voc/Voc^{SQ} was calculated for each device. This ratio is associated to the Voc deficit. The higher the ratio value the lower the Voc deficit. The results show that six compositions had a best device that had a Voc/Voc^{SQ} higher than that of the record 12.6% efficient device (Voc/Voc^{SQ} =58%), but at the highest double alloying was still ~1.9% inferior (10.7% efficient). One issue with the observed data an drawing correlations to the current champion CZTSSe device is that the control CZTSSe device in this study was only half as efficient meaning that our fabrication procedures may need optimization. If optimized making the direct comparison of the alloying effects with a near peer control sample the impact on the research community would be more definitive.

***Table 3**. Summary of Ag, Ge, and Mn substituted CZTSSe photovoltaic device characteristics for various metal substitution conditions. Measurements taken within 24 hours after device fabrication completed with Newport AAA Oriel Sol3A solar simulator emitting 1000 W/m2 at standard conditions (25 °C and AM1.5G).*

	Ag/ (Ag+Cu)	**Mn/ (Mn+Zn)**	**Jsc (mA cm^{-2}**	**Voc (mV)**	**FF (%)**	**PCE (%)**	**Eg (eV)**	V_{oc}/V_{oc}^{SQ}
CZTSSe	**0**	**0**	30 ± 4	385 ± 34	47 ± 5	5 ± 1	1.050	0.47
i	**0.15**	**0**	30 ± 1	397 ± 13	43 ± 2	5.2 ± 0.4	1.103	0.46
ii	**0.15**	**0.08**	31 ± 2	450 ± 12	51 ± 1	5.9 ± 0.3	1.114	0.51
iii	**0.15**	**0.15**	30.5 ± 0.7	524 ± 3	53 ± 2	8.8 ± 0.8	1.118	0.60
iv	**0.15**	**0.22**	30 ± 1	551 ± 3	54 ± 2	9.3 ± 0.2	1.138	0.62
v	**0**	**0.15**	30 ± 1	446 ± 6	41 ± 2	5.5 ± 0.3	1.091	0.51
vi	**0.08**	**0.15**	31 ± 1	531 ± 3	58 ± 3	9.6 ± 0.4	1.090	0.63
vii	**0.22**	**0.15**	31 ± 1	507 ± 2	31 ± 1	6.9 ± 0.3	1.115	0.51
Sample	**Ag/ (Ag+Cu)**	**Ge/ (Ge+Sn)**	**Jsc (mA cm^{-2})**	**Voc (mV)**	**FF (%)**	**PCE (%)**	**Eg (eV)**	V_{oc}/V_{oc}^{SQ}
CZTSSe	**0**	**0**	30 ± 4	385 ± 34	47 ± 5	5 ± 1	1.050	0.47
i	**0.15**	**0**	30 ± 1	397 ± 13	43 ± 2	5.2 ± 0.4	1.103	0.46
viii	**0**	**0.3**	32.5 ± 1.5	513 ± 11	58.5 ± 2	9.8 ± 0.8	1.13	0.58
ix	**0.1**	**0.3**	31.5 ± 1	542 ± 9	48 ± 4	8.3 ± 0.5	1.16	0.59
x	**0.2**	**0.35**	30.5 ± 2	560 ± 7	58 ± 2	10 ± 0.7	1.19	0.59
xi	**0.3**	**0.2**	31 ± 4	522 ± 10	53 ± 4	8.8 ± 0.9	1.21	0.54

The photovoltaic metrics for Ag and Mn alloying is shown in Figure 3-3 below. First of all the Jsc is relatively consistent at 31mA/cm^2 albeit lower than the record IBM device. Based on Voc trends, Figure 3-3 b, there is an apparent maxima between 8-15% Ag/(Ag+Cu) when Mn/(Mn/Zn) is held constant at 15%. However base on the combination of Voc and FF, Figure 3-3 c, trends it appears that if Mn concentration were to be increased in the alloying (while Ag is kept constant at 8-15% Ag/(Ag+Cu)) that there may be further improvement in PCE. It would be interesting for future work to take into account these trends and explore this parameter space to determine if the compositional trend of double cation substitution could be extrapolated as Figure 3-3 suggests.

The photovoltaic metrics for Ag and Ge alloying from Table 3 are plotted in in Figure 3-4 with the added observation that photovoltaic metrics generally improve over time with the Ge as an adduct in CZTSSe. Our measurements of single alloyed Ge CZTSSe agreed with the results of Collord and Hillhouse for freshly fabricated devices, but we were curious to see whether the

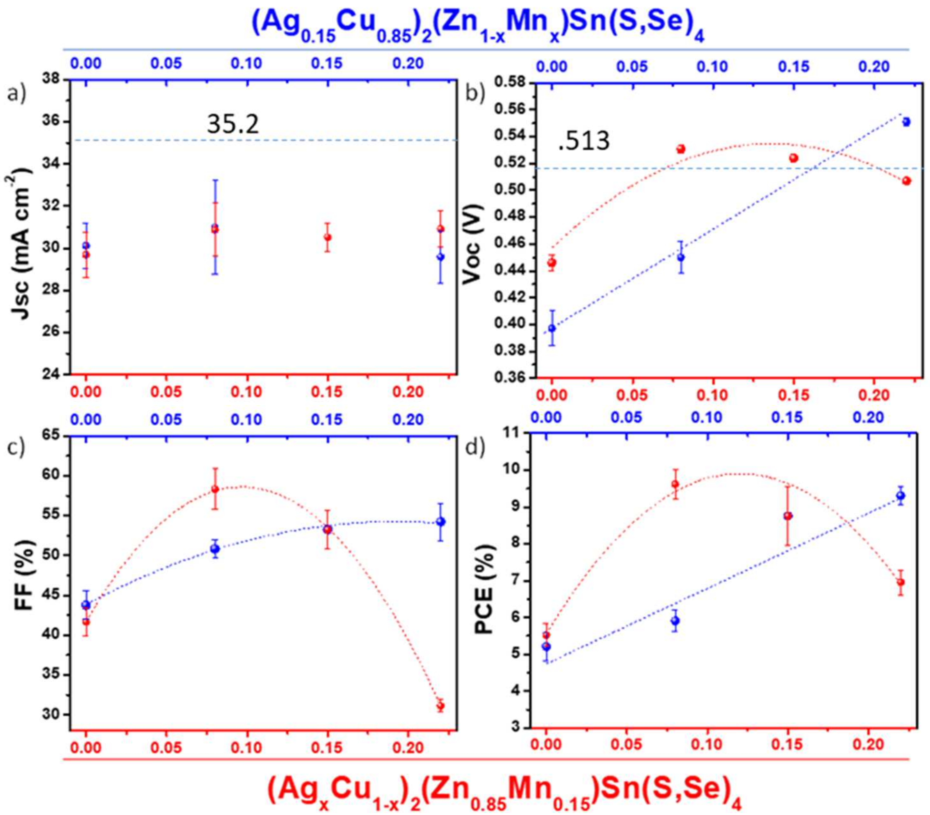

***Figure 3-3**. $(Ag_x,Cu_{1-x})_2(Mn_{0.15},Zn_{0.85})Sn(S,Se)_4$ (red circles) and $(Ag_{0.15},Cu_{0.85})_2(Mn_y,Zn_{1-y})Sn(S,Se)_4$ (blue circles) photovoltaic characteristics for various composition conditions fresh after fabrication. Light blue dotted demarcation line signifies the photovoltaic characteristices of the 2013 IBM record CZTSSe device.*

addition of Ag into the lattice with the double cation substitution approach would affect the observation. The aging observation by Collard and Hillhouse when CZTSSe gradients with the addition of Ge into the lattice the devices seem to increase stability and performance improves following aging in ambient lab conditions [5]. The results of aging once again were observed to be beneficial to photovoltaic metrics across the board and increases were observed until six weeks of aging measurements were conducted and the metrics nearly plateaued. Based on Figure 3-4’s juxtaposition of our experiments with the record CZTS device with aging accounted for the device issue to dethrone the champion seems to indicate the presence of fine grain layers and a conduction band-offset mismatch due to lower FF and Jsc. In the data and highlight in Figure 3-4 is an arrow pointing to a 11.7% PCE $(Ag_{0.2},Cu_{0.8})_2Zn(Ge_{0.35},Sn_{0.65})(S,Se)_4$ device of interenst because upon further analysis it was determined to be not only the highest PCE in this report, but also the highest PCE for a double cation substituted solution-processed (TU/DMF based) CZTS sample ever fabricated by the Hillhouse Group. Figure 3-5 further examines the chacteristics of this device by looking at the JV data at two points in time. It is a positive note that, although the efficienies report are not revolutionary for the research field, the CZTS devices are stable over time unlike the current solution processed perovskite counterparts.

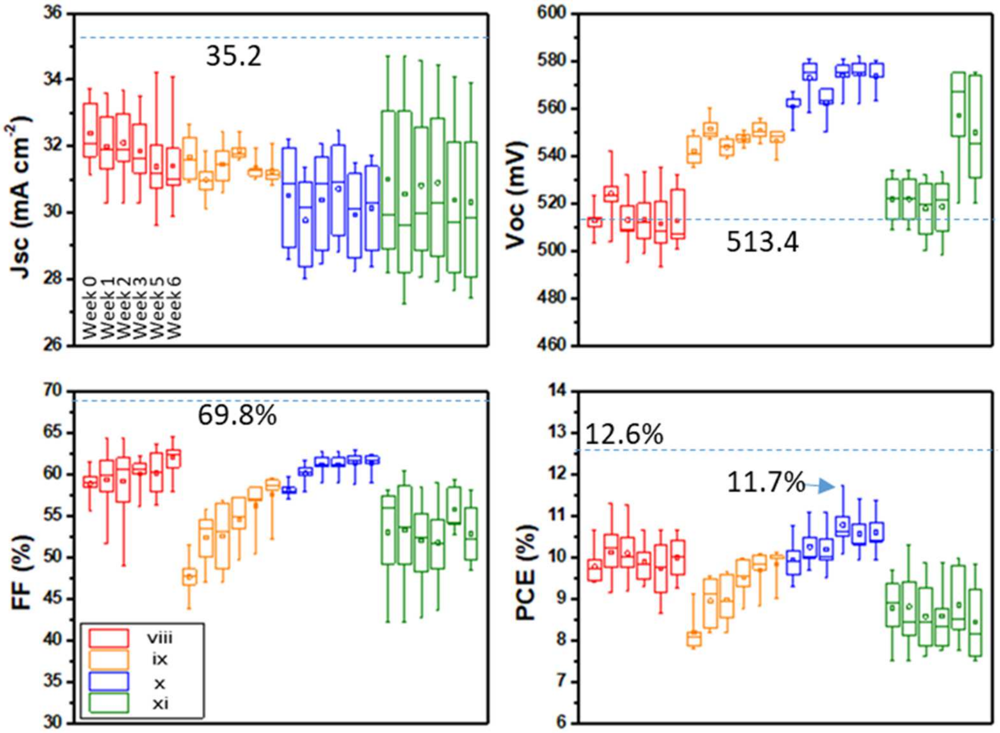

***Figure 3-4**. Photovoltaic characteristics for (viii in red) $Cu_2Zn(Ge_{0.3},Sn_{0.7})(S,Se)_4$, (ix in orange) $(Ag_{0.1},Cu_{0.9})_2Zn(Ge_{0.3},Sn_{0.7})(S,Se)_4$, (x in blue) $(Ag_{0.2},Cu_{0.8})_2Zn(Ge_{0.35},Sn_{0.65})(S,Se)_4$, and (xi in green) $(Ag_{0.3},Cu_{0.7})_2Zn(Ge_{0.2},Sn_{0.8})(S,Se)_4$ measured over time from freshly fabricated (week 0) to week 6. Light blue dotted demarcation line signifies the photovoltaic characteristices of the 2013 IBM record CZTSSe device.*

In the study's champion device the 1% PCE improvement seems driven by the three fold increase of the shunt resistance that likely improved the FF an additional 3%. The Voc from new to aged increased 1% which is approximately the same observation for Collord's Ge single alloyed devices. Although it was not the goal of this report to study the mechanics as to why this phenomena is observed the apparent cost of receiving this benefit is only time. Collord hypothesized that the aging phenomena could be attributable to either slow diffusion of defects in the lattice, oxygenation, or migration of defects caused by the electric field formed by the p-n junction. It would be very interesting for future work to understand this phenomena as it could be crucial for understanding and engineering defect free CZTSSe. The performance of the 11.7% efficient device shows is that with additional optimization tuning this work could result in a new CZTSSe record.

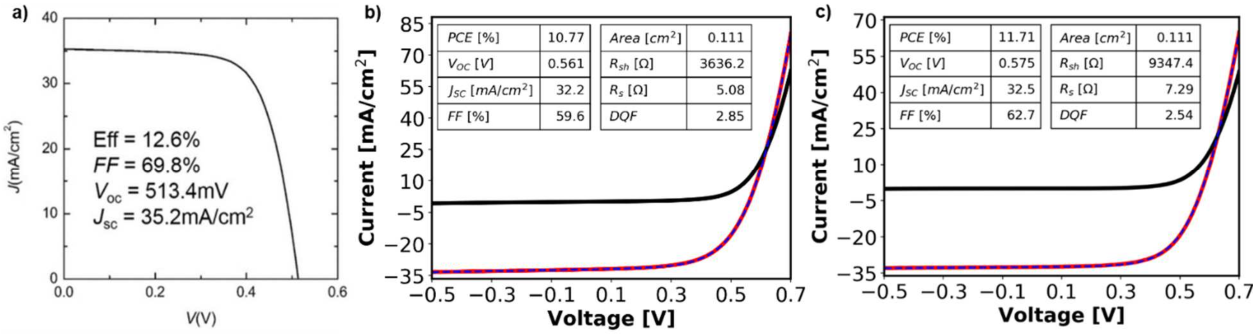

Figure 3-5. *CZTS JV curves of interest: a) current champion device by IBM in 2013 using solution processed hydrazine method [2], b) $(Ag_{0.2},Cu_{0.8})_2Zn(Ge_{0.35},Sn_{0.65})(S,Se)_4$ device measured within 24 hours of fabrication, and c) Highest PCE device, 11.7% (Voc/VocSQ=62.2%), measured after four weeks of ambient aging.*

3.4 Defect Passivation Characterization

To help explain the increase in performance from the CZTSSe control sample we investigated further into details of the measurements taken during characterization. First, from the Ag + Mn UV-Vis transmittance spectral data, the Urbach tail energy (E_u) was extracted by the inverse of the slope from the linear region below Eg from the plot ln(α) *versus* photon energy (hv) (Figure 6). The results reveal that the E_u decreases with alloying CZTSSe with both Ag and Mn. The Urbach energy tail is for the CZTSSe films with the highest concentrations of Ag and Mn, $(Ag_{0.15},Cu_{0.85})_2(Mn_{0.22},Zn_{0.78})Sn(S,Se)_4$, where E_u is equal to 10.4 meV and compared with the Voc/Voc^{SQ} calculations from Table 3.

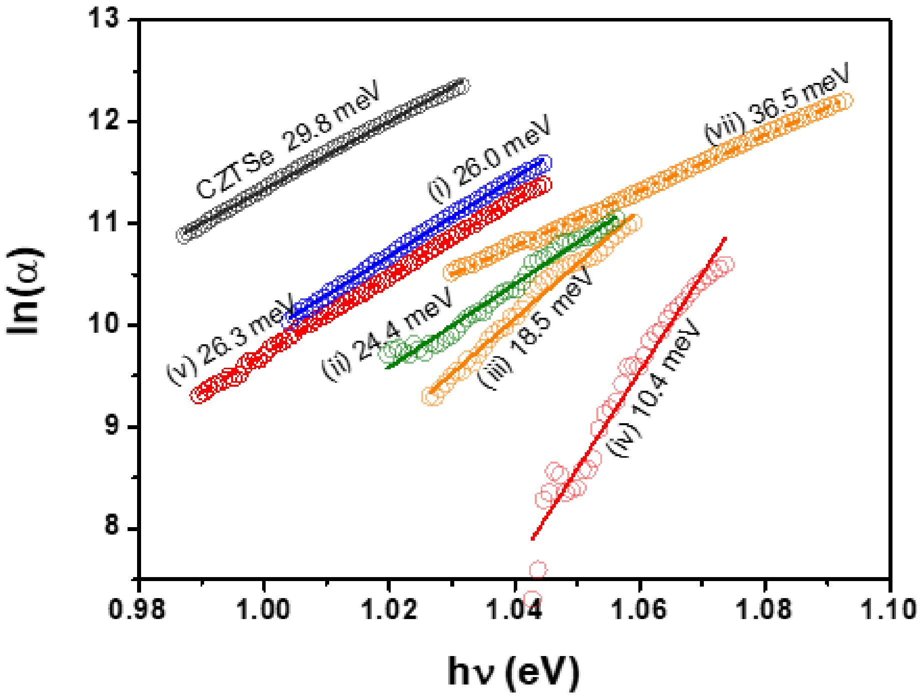

Figure 3-6. *Urbach tail plots for the CZTSe, $(Ag_x,Cu_{1-x})_2(Mn_{0.15},Zn_{0.85})Sn(S,Se)_4$ and $(Ag_{0.15},Cu_{0.85})_2(Mn_z,Zn_{1-z})Sn(S,Se)_4$ films.*

When E_u is plotted versus Voc/Voc^{SQ} (Figure 3-7) it is observed that nearly linearly that when E_u decreases, Voc/Voc^{SQ} increases. By examining the compositional changes in the Urbach Energy we are observing differences in absorber quality. Based on this analysis compositions (iii) $(Ag_{0.15},Cu_{0.85})_2(Mn_{0.15},Zn_{0.85})Sn(S,Se)_4$ and (iv) $(Ag_{0.15},Cu_{0.85})_2(Mn_{0.22},Zn_{0.85})Sn(S,Se)_4$ had less recombination losses as compared to un-alloyed and the single-alloyed controls. This suggests that higher concentrations of Mn (20-30%) are beneficial for an alloyed approach. Ag and Ge alloyed samples were not measured with UV-Vis so a similar comparison cannot be drawn, but if the experiments were to be repeated it would be interesting data to calculate for alloys of CZTS with Ge+Mn or Ag+Ge+Mn.

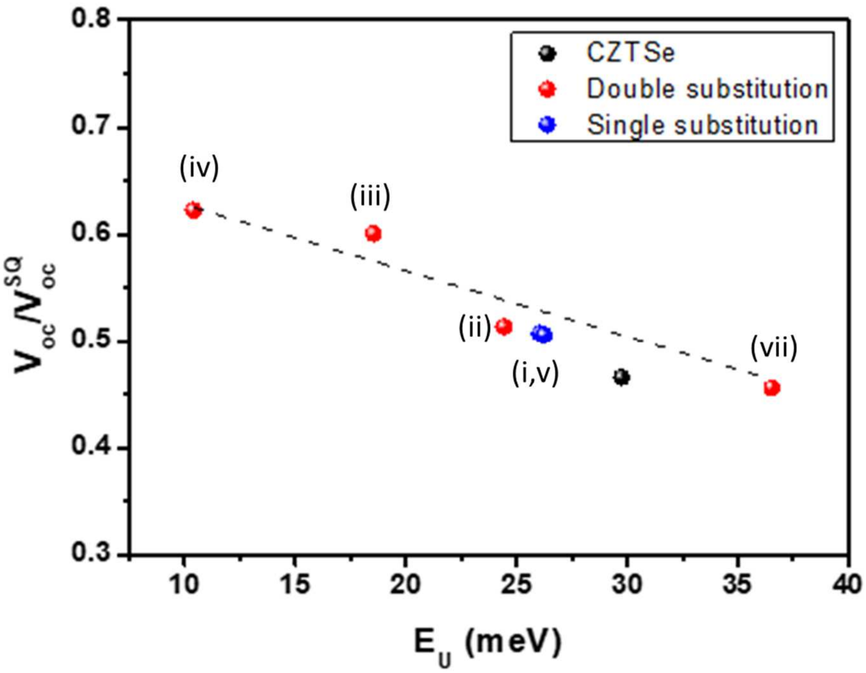

Figure 3-7. *Relationship between Urbach Energy and Voc/Voc*^{SQ} *for the CZTSe ,* $(Ag_x,Cu_{1-x})_2(Mn_{0.15},Zn_{0.85})Sn(S,Se)_4$ *and* $(Ag_{0.15},Cu_{0.85})_2(Mn_z,Zn_{1-z})Sn(S,Se)_4$ *films.*

Originally Raman spectra had been collected as an alternate means to quantify the impurities associated with the presence by quantifying the D- and G-bands, however the work by Dimitrievska et al. suggested that if we reexamined the “fingerprint” region in the Raman spectra to see the effectiveness of the defect passivation alloying approach. In a CZTSSe Raman spectra the prominent peak at 196 cm^{-1} corresponds to Se vibrations in the lattice, the peak at 170 cm^{-1} correlates experimentally to the $[Zn_{Cu}+V_{Cu}]$ defect clusters, and the peak at 250 cm^{-1} correlates experimentally to $[2Zn_{Cu}+Zn_{Sn}]$ defect clusters [15]. Examining the effects of Ag alloying in Figure 3-8, the deconvoluted spectra exhibits a small increase in $[Zn_{Cu}+V_{Cu}]$ defect clusters and a small decrease in Cu_{Zn} point defects, which can also propagate at the 250 cm^{-1} region [16]. A reduction in Cu_{Zn} point defects via the mechanism if Ag substitution with Cu would support the single alloying hypothesis. What is concerning in the Raman results is that if we examine cases Mn is alloyed a sixth deconvoluted peak is present Figure 3-8 v) and iii). This additional peak may be the result of a secondary phase possibly MnSe that was undetected without refinement in XRD. MnSe is seen at 2θ’s close to that of the 112 plane and may be convoluted. The presence of MnSe, with a band gap energy from 1.13-1.25eV, could be detrimental to CZTSSe band gap engineering for band gaps higher than our CZTSSe targeted 1.13eV may observe increased sub-band gap absorption and recombination losses [17]. From this analysis the qualification to say Mn reduces the concentration of these defect clusters in the lattice is not apparent (these defect clusters appear to increase in concentration), but since the Voc and PCE gains previously shown the benefits to incorporating Mn must be attributed to improved interfacial recombination.

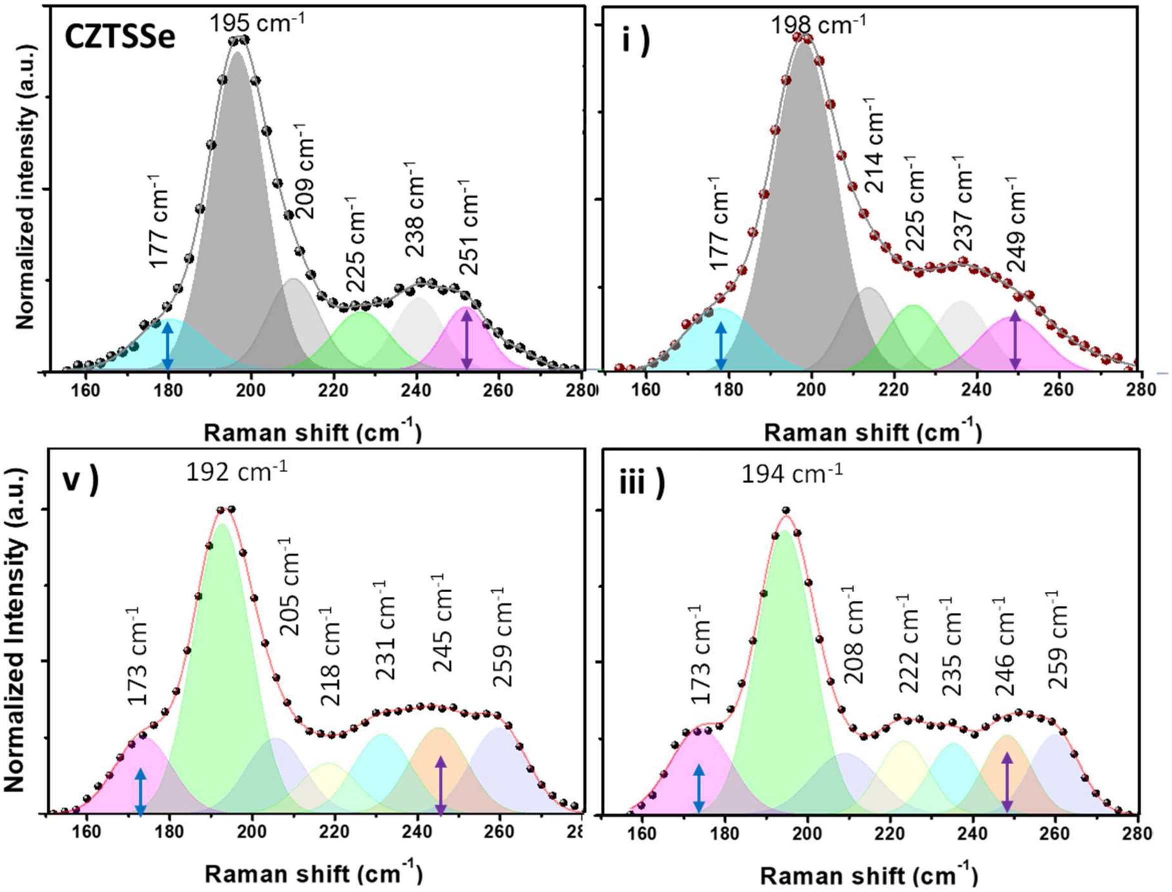

Figure 3-8. Raman spectra with deconvoluted peaks of the films of CZTSSe (i) $(Ag_{0.15},Cu_{0.85})_2ZnSn(S,Se)_4$, (v) $Cu_2(Mn_{0.15},Zn_{0.85})Sn(S,Se)_4$, and (iii) $(Ag_{0.15},Cu_{0.85})_2(Mn_{0.15},Zn_{0.85})Sn(S,Se)_4$. The blue arrow corresponds the CZTSSe control height of the ~170 cm^{-1} peak and the purple arrow corresponds to the CZTSSe control height of the ~250 cm^{-1} peak. The blue and purple height demarcations are transcribed onto the adjacent alloyed Raman spectra in order to visualize changes in heights.

Next when we examine the Raman spectra of Ag and Ge incorporated CZTSSe, as shown in Figure 3-9, the peak at 250 cm^{-1} nearly disappears with the presence of Ge in the lattice as compared to the control and the Ag alloyed. This may be attributable to Ge alone although originally thought to correlate to the addition of Ag. Since the Voc dramatically improves with the addition of Ge the 250 cm^{-1} peak may have more relation to a Sn point defect or a Sn defect cluster since those defects are estimated to be deeper sub-band gap defects.

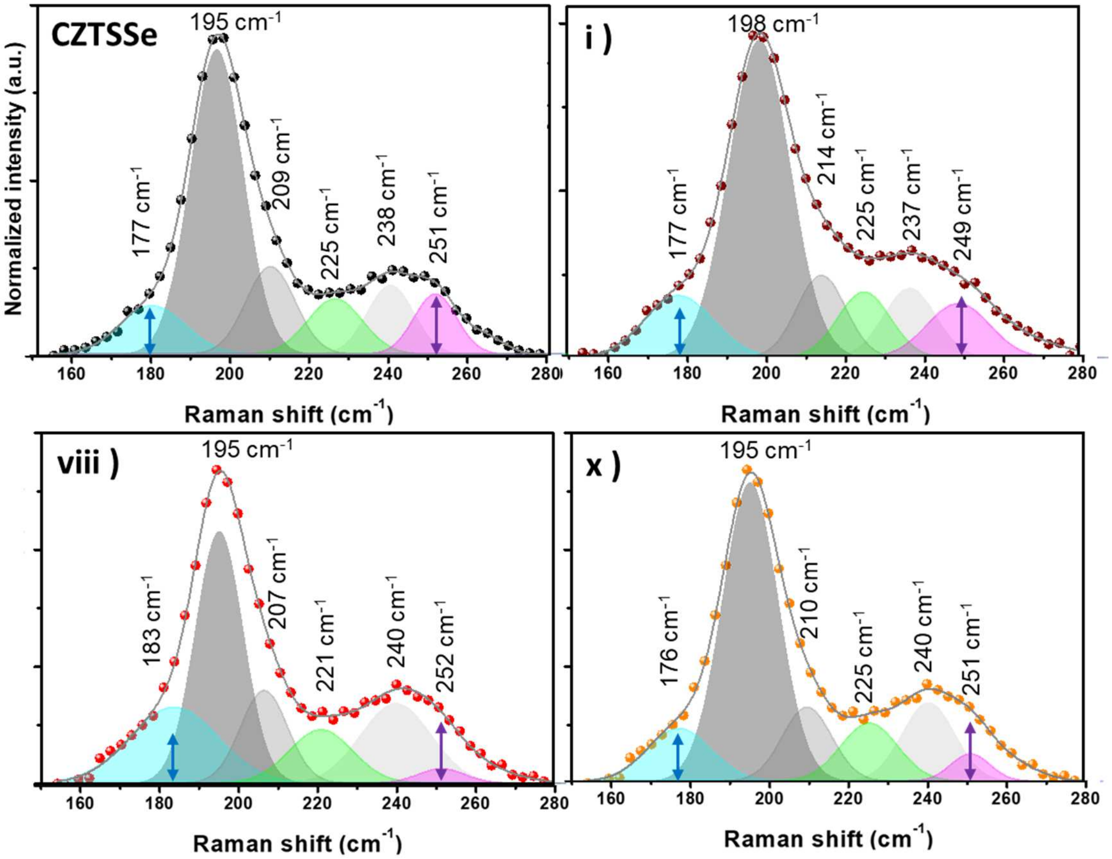

Figure 3-9. Raman spectra with deconvoluted peaks of the films of CZTSSe (i) $(Ag_{0.15},Cu_{0.85})_2ZnSn(S,Se)_4$, (viii) $Cu_2Zn(Ge_{0.3},Sn_{0.7})(S,Se)_4$, and (x) $(Ag_{0.2},Cu_{0.8})_2Zn(Ge_{0.35},Sn_{0.65})(S,Se)_4$. The blue arrow corresponds the CZTSSe control height of the ~170 cm^{-1} peak and the purple arrow corresponds to the CZTSSe control height of the ~250 cm^{-1} peak. The blue and purple height demarcations are transcribed onto the adjacent alloyed Raman spectra in order to visualize changes in heights.

4. Conclusions

The challenge of engineering an improved CZTSSe absorber layer is not trivial because so little is still known about the physical and chemical processes that govern the stoichiometry and that the formation of detrimental defects is usually favored. Taking an approach with solution processed thin-films research may not be the most accurate and reliable method with so many unknowns yet to discover and such delicate details are required to assess the impact of a small change. This method is cost effective way for high throughput exploration with the expectation that there will be a low rate of reportable success. A method using photoluminescence to measure CZTSSe/CdS substrates to model defect concentrations as the stoichiometry is altered would be excellent means to screen in a high throughput environment. A method employed in this nature would have additional cost savings by avoiding fabricating devices that have high likelihood to have low performance.

This study was unsuccessful in fabricating a device that had a higher efficiency then the 2013 IBM device, but it was comprehensive in applying multiple different aspects in field literature. Double cation substitutions seem to have promise for the advancement of CZTSSe, but based on the results either the cations chosen were not in the correct proportion or triple cation substitution may be necessary in order attack different hindrances in CZTSSe stoichiometry. If I were to conduct the experiments again I would consider increasing the double cation substitution compositional parameter space and also design the alloying with smaller compositional changes like a gradient in order to see the mechanics clearer.

Finding a composition that achieves an efficiency greater than 15% is the penultimate step towards making CZTSSe a viable industrial consideration. The positive impacts of Sn replacement with Ge still remain irrefutable, but I believe that understanding why aging Ge incorporated CZTSSe is beneficial to device performance may unlock valuable physical and chemical processes fundamental to understanding CZTSSe defect chemistry. If given more time to conduct experimentation, discovering if any other cation substitutions display this result due to aging may also be impactful. From our results and current understanding the direction to take with these substitutions would be to continue experimentation with all three discussed cations. It is also imperative that if the design for testing is to include making devices that fine-grain layers be investigated as result of the current fabrication steps. If identified and not removed by optimizing the fabrication procedures all results in the future will continue to be hindered in performance.

5. References.

1. Powell, D. M., Ran Fu, K., Horowitz, P. A., Basore, M. W. & Buonassisi, T. The Capital Intensity of Photovoltaics Manufacturing: Barrier to Scale and Opportunity for Innovation. Energy & Environ. Sci. 8, 3395–3408 (2015).

2. Wang, W., Winkler, M. T., Gunawan, O., Gokmen, T., Todorov, T. K., Zhu, Y. & Mitzi, D. B. Device Characteristics of CZTSSe Thin-Film Solar Cells with 12.6% Efficiency. Adv. Energy Mater. 4, 1301465 (2014).

3. Shockley, W. & Queisser, H. J. Detailed Balance Limit of Efficiency of p-n Junction Solar Cells. J. Appl. Phys. 32, 510 (1958).

4. Chen, S., Walsh, A., Gong, X.-G. & Wei, S.-H. Classification of lattice defects in the kesterite Cu2ZnSnS4 and Cu2ZnSnSe4 earth-abundant solar cell absorbers. Adv. Mater. 25, 1522–1539 (2013).

5. Collord, A. D. & Hillhouse, H. W. Germanium Alloyed Kesterite Solar Cells with Low Voltage Deficits. Chem. Mater. 28, 2067–2073 (2016).

6. Qi, Y.-F., Kou, D.-X., Zhou, W.-H., Zhou, Z.-J., Tian, Q.-W., Meng, Y.-N., Liu, X.-S., Du, Z.-L. & Wu, S.-X. Engineering of interface band bending and defects elimination via a Ag-graded active layer for efficient (Cu,Ag)2ZnSn(S,Se)4 solar cells. Energy & Environ. Sci. 10, (2014).

7. Li, J., S. Y. Kim, D. Nam, X. Liu, J. H. Kim, H. Cheong, W. Liu, H. Li, Y. Sun and Zhang, Y.. Control of Zn Content and Influence on Cu2ZnSnSe4 Thin-Film Solar Cells Fabricated by Coevaporation. *Sol. Energy Mater. Sol. Cells*, 2017, 159, 447–455.

8. Gong, W., Tabata, T., Takei, K., Morihama, M., Maeda, T. & Wada, T. Crystallographic and optical properties of (Cu, Ag)2ZnSnS4and (Cu, Ag)2ZnSnSe4solid solutions: Crystallographic and optical properties of (Cu, Ag)2ZnSnS4and (Cu, Ag)2ZnSnSe4solid solutions. Phys. Status Solidi 12, (2015).

9. Clark, J.A., Uhl, A. R., Martin, T. R., Hillhouse, H. W. Evolution of Morphology and Composition during Annealing and Selenization in Solution-Processed Cu_2ZnSn(S,Se)4. Chem. Mater. 2017, 29, 9328.

10. Collord, A. D., Xin, H. & Hillhouse, H. W. Combinatorial Exploration of the Effects of Intrinsic and Extrinsic Defects in Cu2ZnSn(S,Se)4. IEEE J. Photovoltaics 5, 2015.

11. Guo, Q., Kim, S. J., Kar, M., Shafarman, W. N., Birkmire, R. W., Stach, E. A., Agrawal, R. & Hillhouse, H. W. Development of CuInSe2 nanocrystal and nanoring inks for low-cost solar cells.Nano Lett. 8, 2982–2987 (2008).

12. Bosson, C. J., Birch, M. T., Halliday, D. P., Knight, K. S., Gibbs, A. S., and Hatton, P. D.. Cation disorder and phase transitions in the structurally complex solar cell material Cu2ZnSnS4. *J. Mater. Chem. A*, 2017, 5, 16672–16680.

13. Fairbrother, A., García-Hemme, E., Izquierdo-Roca, V., Fontané, X., Pulgarín-Agudelo, F.A., Vigil-Galán, O., Pérez-Rodríguez, A., and Saucedo, E.. Development of a Selective Chemical Etch To Improve the Conversion Efficiency of Zn-Rich Cu2ZnSnS4 Solar Cells. *J. Am.*

Chem. Soc., 2012, 134, 8018–8021.

14. Clark, J. A., Murray, A., Lee, J. M., Autrey, T. S., Collord, A. D., and Hillhouse, H. W.. Complexation Chemistry in N,N-Dimethylformamide-Based Molecular Inks for Chalcogenide Semiconductors and Photovoltaic Devices. *J. Am. Chem. Soc.*, 2019, 141, 298–308.

15. Dimitrievska, M., Fairbrother, A., Saucedo, E., Pérez-Rodríguez, A., and Izquierdo-Roca, V.. Secondary Phase and Cu Substitutional Defect Dynamics in Kesterite Solar Cells: Impact on Optoelectronic Properties. *Sol. Energy Mater. Sol. Cells*, 2016, 149, 304–309.

16. Dimitrievska, M., Fairbrother, A., Saucedo, E., Pérez-Rodríguez, A., and Izquierdo-Roca, V.. Influence of compositionally induced defects on the vibrational properties of device grade Cu2ZnSnSe4 absorbers for kesterite based solar cells. Applied Phys. Letters, 2015, 106.

17. Kariper, I.A. A New Route to Synthesize MnSe Thin Films by Chemical Bath Deposition Method. Materials Research, 2018, 21.